HHS Public Access

Author manuscript

IEEE Trans Med Imaging. Author manuscript; available in PMC 2016 November 01.

Published in final edited form as:

IEEE Trans Med Imaging. 2015 November ; 34(11): 2354–2365. doi:10.1109/TMI.2015.2432797.

Comparison of Acoustic Radiation Force Impulse Imaging Derived Carotid Plaque Stiffness with Spatially Registered MRI Determined Composition

Joshua R. Doherty,
Department of Biomedical Engineering, Duke University, Durham, NC.

Jeremy J. Dahl,
Department of Radiology, Stanford University, Stanford, CA.

Peter G. Kranz,
Department of Radiology, Duke University Medical Center, Durham, NC.

Nada El Husseini,
Department of Neurology, Duke University Medical Center, Durham, NC.

Hing-Chiu Chang,
Department of Radiology, Duke University Medical Center, Durham, NC. They are also with Brain Imaging and Analysis Center, Duke University Medical Center, Durham, NC.

Nan-kuei Chen,
Department of Radiology, Duke University Medical Center, Durham, NC. They are also with Brain Imaging and Analysis Center, Duke University Medical Center, Durham, NC.

Jason D. Allen,
Department of Cardiology, Duke University Medical Center, Durham, NC. He is also with the Department of Community and Family Medicine, Duke University Medical Center, Durham, NC.

Katherine L. Ham, and
Department of Cardiology, Duke University Medical Center, Durham, NC.

Gregg E. Trahey
Department of Biomedical Engineering, Duke University, Durham, NC. He is also with the Department of Radiology, Duke University Medical Center, Durham, NC.

Abstract

Measurements of plaque stiffness may provide important prognostic and diagnostic information to help clinicians distinguish vulnerable plaques containing soft lipid pools from more stable, stiffer plaques. In this preliminary study, we compare *in vivo* ultrasonic Acoustic Radiation Force Impulse (ARFI) imaging derived measures of carotid plaque stiffness with composition determined by spatially registered Magnetic Resonance Imaging (MRI) in five human subjects with stenosis >50%. Ultrasound imaging was implemented on a commercial diagnostic scanner with custom pulse sequences to collect spatially registered 2D longitudinal B-mode and ARFI images. A standardized, multi-contrast weighted MRI sequence was used to obtain 3D Time of Flight (TOF), T1 weighted (T1W), T2 weighted (T2W), and Proton Density Weighted (PDW) transverse image stacks of volumetric data. The MRI data was segmented to identify lipid,

calcium, and normal loose matrix components using commercially available software. 3D MRI segmented plaque models were rendered and spatially registered with 2D B-mode images to create fused ultrasound and MRI volumetric images for each subject. ARFI imaging displacements in regions of interest (ROIs) derived from MRI segmented contours of varying composition were compared. Regions of calcium and normal loose matrix components identified by MRI presented as homogeneously stiff regions of similarly low (typically ≈ 1μm) displacement in ARFI imaging. MRI identified lipid pools >2mm^2, found in three out of five subjects, presented as softer regions of increased displacement that were on average 1.8 times greater than the displacements in adjacent regions of loose matrix components in spatially registered ARFI images. This work provides early evidence supporting the use of ARFI imaging to noninvasively identify lipid regions in carotid artery plaques *in vivo* that are believed to increase the propensity of a plaque to rupture. Additionally, the results provide early training data for future studies and aid in the interpretation and possible clinical utility of ARFI imaging for identifying the elusive vulnerable plaque.

Index Terms

Ultrasound; MRI; Multi-modality fusion; Vessels

I. Introduction

THE rupture of atherosclerotic plaques is a major cause of stroke [1], the fourth leading cause of death and number one cause of long-term disability in the United States [2]. Unfortunately, traditional measurements of arterial stenosis can only diagnose atherosclerotic plaque burden late in the course of disease and are only partially effective in predicting ischemic events. These facts may explain why a large number of high-risk atherosclerotic plaques go undetected [3]. There is a clear unmet clinical need for a diagnostic method that can provide an earlier assessment of a plaque's risk of rupture before the onset of clinical events.

Based on retrospective analysis of histological data [4–7], the so-called "vulnerable" plaque that is more susceptible to rupture is characterized by a thin fibrous cap and a large lipid pool. The presence of a lipid pool is particularly dangerous because its low stiffness – the ability of a material to resist deformation – is considerably lower than the stiffness of normal arterial tissue. In general, Young's Modulus values of vulnerable lipid components (0.5 – 50 kPa) are at least an order of magnitude smaller than those reported in the literature for normal arterial tissue (500 kPa – 2000 kPa) and even stiffer fibrous and calcified components (>2000 kPa) [8–10]. Computational modeling studies have shown the low stiffness of lipid pools makes them unable to support stresses induced by blood pressure, causing regions of stress concentration within the overlying stiff fibrous cap that corresponded to sites of rupture [11].

The development of diagnostic imaging methods to noninvasively distinguish vulnerable from stable carotid plaques *in vivo* is an area of intense research activity [12,13]. MRI methods have received much attention in particular with the development of multi-contrast

weighted sequences that can differentiate lipid, fibrous, calcified, hemorrhagic, and thrombotic regions *in vivo* [14–20]. Despite high sensitivity and specificity (95% and 76% for the lipid-rich necrotic core, 84% and 91% for calcification, 87% and 84% for hemorrhage, and 79% and 77% for loose matrix components, respectively, for regions > $2mm^2$ [17]) the high equipment costs and long acquisition times may limit the use of MRI as a routine screening method.

Given the high degree of contrast in stiffness that exists between stable normal arterial tissue and vulnerable soft lipid pools, it seems likely that an imaging method capable of characterizing plaque stiffness may help clinicians identify the elusive vulnerable plaque. Ultrasound-based acoustic radiation force elasticity imaging methods are an emerging technology that may fit this niche [21]. Unlike conventional B-mode imaging that differentiates features with dissimilar acoustic properties (e.g. density and speed of sound), elasticity imaging methods differentiate features and/or structures with different mechanical (e.g. elastic, damping, and inertial) properties and thereby provide a fundamentally different source of imaging contrast.

One method, Acoustic Radiation Force Impulse (ARFI) imaging [22], is particularly attractive for carotid plaques because it can be performed on conventional ultrasound scanners during routine, noninvasive carotid duplex examinations. Briefly, the technique applies a localized impulsive acoustic radiation force excitation and then measures the induced displacements both temporally and spatially. In general, soft tissues displace more and take longer to recover than stiffer tissue. Computational finite element method simulations showed ARFI imaging can differentiate lipid pools from the fibrous cap and normal media components and that ARFI imaging induced stresses on fibrous caps are three orders of magnitude lower than the stresses induced by blood pressure [23]. Preliminary ARFI imaging studies in vascular tissue showed regions of low displacement in ARFI images correlated with histologically identified collagen and elastic content *in vivo* [24] and *ex vivo* [25] in porcine iliac arteries. Soft regions of high displacement on the other hand have been associated with histologically confirmed lipid-filled regions in an *ex vivo* human popliteal artery [26]. Dahl et al. [27] showed carotid plaques that were heterogeneous in B-mode imaging contained regions of varying stiffness in ARFI imaging, whereas homogeneous plaques in B-mode were generally homogeneous in ARFI imaging. Despite the promising results demonstrated in these early studies, to date no spatially registered *in vivo* validation effort in human subjects has been reported.

The goal of this preliminary study is to compare *in vivo* ARFI imaging derived carotid plaque stiffness with composition determined by spatially registered MRI in human subjects.

II. Materials & Methods

A. Study Population

Five subjects (mean age 74; SD 7.7; 2 males & 3 females) (Table I) with carotid artery stenosis > 50%, determined by CT angiograms and/or ultrasound imaging, were recruited to undergo an ultrasound exam and MRI exam according to an Institutional Review Board (IRB) approved protocol with written informed consent. The MRI exam was performed

within 1 hour following the ultrasound exam in Subjects 1, 3, and 4. Due to scheduling conflicts, the MRI exams for Subject 2 and Subject 5 were acquired three weeks and 6 months, respectively, following the ultrasound exam.

B. Ultrasound (B-mode & ARFI) Imaging

1) Imaging Protocol—Ultrasonic B-mode and ARFI imaging was implemented on a diagnostic ACUSON S2000™ ultrasound scanner with a 9L4 linear array transducer (Siemens Medical Solutions USA, Inc., Issaquah, WA). A standard B-mode examination was performed by a trained sonographer with the subjects lying in the supine position and their head slightly tilted to facilitate access of the ultrasound probe. Guided by real-time B-mode imaging, the transducer was swept across the neck to assess the overall extent of atherosclerotic plaque burden and to identify viewing angles, reported with respect to the anterior–posterior axis with posterior oriented at 0°, and locations (typically 2–3) where image quality was best. At each of these locations and/or angles 5–10 B-mode/ARFI datasets were acquired using previously developed custom pulse inversion (PI) harmonic imaging sequences that collect spatially matched B-mode and ARFI information within a single acquisition at a combined frame rate of 4.8 Hz [28]. A high-quality B-mode image that was displayed by the scanner with optimized gain profiles and display settings not included in the custom B-mode/ARFI pulse sequence was saved prior to each data acquisition. Images were acquired in the transverse and longitudinal planes; however, due to poor ARFI image quality in the transverse orientation, only the longitudinal planes are shown herein.

The custom B-mode imaging sequence consisted of 256 A-lines distributed across a 40 mm field-of-view (FOV) and the ARFI imaging sequence consisted of 50 A-lines distributed across a 15mm FOV. Each ARFI imaging A-line is composed of a single acoustic radiation force excitation pulse (push beam) that displaces the tissue and a series of conventional imaging pulses (track beams) that monitor the deformation from 0.7msec before to 2.6 msec after the acoustic radiation force excitation at a pulse repetition frequency of 9.4 kHz. A “non-push” ARFI frame that included identical A-line tracking ensembles of the standard “push” ARFI frame but not the ARFI push beam was collected immediately following each “push” ARFI frame to monitor non-ARFI induced motion. The specific pulse characteristics for B-mode and ARFI imaging are listed in Table II.

Raw radiofrequency (RF) data was acquired via the Axius Direct™ Ultrasound Research Interface (Siemens Medical Solutions USA, Inc., Issaquah, WA) at 40MHz and processed off-line with MATLAB™ (The MathWorks, Natick, MA) software.

2) Data & Image Processing—Axial displacements were measured using normalized cross-correlation (NCC) with a 1.5λ axial kernel and 0.5λ axial search region. Quadratic based motion filters were used to remove artifacts from non-ARFI induced axial motion including physiologic and transducer motion [29]. Performance of the motion filters was assessed in the “non-push” ARFI imaging frame. Poor quality displacement estimates with a NCC value less than a threshold (typically 0.99) were set to transparent in the ARFI images. A 0.5×0.5 mm median filter was applied to the ARFI images which depict the maximum

axial displacements measured within a temporal window (typically 0.35 to 0.75msec.) immediately following the cessation of the acoustic radiation force excitation. Remaining noise within the arterial lumen not removed by the NCC threshold was removed using a mask segmented from the spatially registered B-mode image.

C. Magnetic Resonance Imaging (MRI)

1) Imaging Protocol—Magnetic Resonance (MR) images of the carotid artery were obtained using a 3.0T GE Discovery MR750 scanner (GE Healthcare, Waukesha, WI) with an 8 channel neurovascular phased array coil according to a multi-contrast weighted standardized protocol [19] that has been validated in the literature [17–19]. This imaging protocol consisted of: 1) 3D Time-of-flight (TOF), 2) T1-weighted (T1W) double-inversion-recovery (DIR) fast spin echo (FSE), 3) T2-weighted (T2W) FSE, and 4) proton density-weighted (PDW) FSE sequences. Fat suppression was used to reduce signal from subcutaneous tissues with the no phase wrap parameter to prevent aliasing of objects outside the FOV. A finger pulse oximeter was used for cardiac gating. Specific scanning parameters for the MRI acquisition are listed in Table III.

Images were acquired in the transverse plane with a 16 × 16 cm FOV. The voxel size for the T1W, PDW, and T2W scans was 0.63 × 0.63 × 2.0 mm and for the TOF scan it was 0.31 × 0.31 × 0.5 mm. In the TOF scan, 80 slices (40mm) were obtained. With relatively long acquisition times, the T1W, T2W, and PDW scans were limited to 10 slices (20mm). The total MRI examination time including setup, localizer, and calibration scans ranged between 60 and 90 minutes. To ensure alignment, the MRI acquisition was positioned according to the distance from the carotid bifurcation to the plaque measured during the ultrasound exam.

2) Segmentation & 3D Model Rendering—Individual 2D MR images were segmented by a trained technician and radiologist that were blinded to the B-mode and ARFI images using MRI-PlaqueView™ software (VP Diagnostics, Seattle, WA). A semi-automated boundary detection tool was utilized to segment the lumen and outer vessel wall in the software, which then compared signal intensities across the spatially matched TOF, T1W, T2W, and PDW images to identify lipid-rich necrotic core, calcium, loose matrix, and lumen components. The 2D segmented image stack was converted into DICOMs using Osirix® [?], then imported into 3D Slicer [?] and smoothed using a Laplacian algorithm to render 3D models of the segmented plaque components.

D. Ultrasound & MRI Image Registration

For each subject, a single B-mode/ARFI ultrasound image was spatially registered with the MRI data according to the routine in Figure 1. The representative B-mode/ARFI image for each subject was selected by first choosing the location and/or angle with the best B-mode image quality, based qualitatively on conspicuity of the lumen–arterial wall boundary, and largest plaque volume. Then, considering the 5–10 datasets recorded at this location/angle, the image pair with the most temporally and spatially consistent features in ARFI imaging was selected. In general, small differences were observed in ARFI images acquired at a single location. The B-mode image from this pair was then spatially registered with the high-resolution 3D TOF volume containing the 3D segmented plaque model. Image

registration was performed manually in 3D Slicer [?], taking advantage of the ability to: 1) apply spatial transformations to imported image data, 2) view arbitrary (i.e. non-cartesian) planes, and 3) overlay multiple images and volumes simultaneously with transparencies to confirm spatial alignment. In addition to plaque geometry and size, features including the location of the carotid bifurcation (BIF) and the diameters of the common carotid artery (CCA), external carotid artery (ECA), and internal carotid artery (ICA) visualized in both the B-mode and 3D TOF images were used to confirm proper alignment. With the 3D TOF dataset spatially registered to the rendered 3D segmented MRI plaque volume and also the 2D B-mode image that is registered with the 2D ARFI image, the 3D segmented MRI plaque volume was effectively registered with the B-mode/ARFI image pair. Final images showing the overlaid contours of the rendered 3D segmented MRI plaque model on both the 2D B-mode image and the 2D ARFI image overlaid on the B-mode image were created.

Despite the subjectivity in choosing the most representative image pair from all the B-mode/ARFI images collected, the results are semi-blinded because the ARFI image was not used during the registration process. Instead, the 3D segmented MRI regions depicting plaque composition were compared with the ARFI derived plaque stiffness only after the spatial registration was complete.

E. Comparing ARFI imaging plaque stiffness with MRI composition

To compare ARFI imaging displacements between regions of varying composition identified by MRI, regions of interest (ROIs) based on the overlaid contours of the segmented MRI plaque volume were defined in the ARFI image. These ARFI imaging ROIs were defined by first overlaying the MRI segmented contours of composition on the ARFI image. In some cases the coarse 2mm resolution of MRI in the longitudinal B-mode/ARFI imaging plane resulted in MRI segmented contours that extended outside the arterial wall into the lumen and/or surrounding tissue in the B-mode/ARFI images. To compensate for this and small mis-registration errors, non-rigid, manual adjustments <1mm were then allowed to smooth the overlaid MRI derived contours in defining the ARFI ROIs. Additionally, only MRI segmented regions > $2mm^2$ were included in the ARFI imaging ROI analysis as high sensitivity and specificity of MRI has only been reported for carotid plaque regions of this size [17]. The mean and standard deviation of the ARFI imaging displacements in the ROIs was determined in the near and far wall for each subject.

III. Results

An analysis of the B-mode, ARFI, and MR images for Subjects 1–5 are presented in a case study format in the following section. While visual comparisons of ARFI imaging are made with respect to the 3D segmented plaque model contours (solid lines) overlaying the B-mode images, the mean and standard deviation of displacements in the ARFI ROIs (dashed lines) overlaying the ARFI images that were derived from segmented MRI contours >$2mm^2$ are reported.

A more detailed analysis for Subject 1 is included to fully describe the image acquisition and registration process that was used to ultimately compare the MRI and ARFI imaging data. For conciseness, only 1) the spatially registered B-mode image with overlaid segmented

MRI plaque model contours and 2) the ARFI image, overlaid on the B-mode image, with the ARFI ROIs derived from the segmented MRI plaque model contours are shown for Subjects 2–5. High quality B-mode images displayed by the ultrasound scanner during the exam are shown for Subjects 2–5 in Figure 2 to provide an overview of the plaque burden. For reference, Table IV lists the B-mode and ARFI image acquisition and processing parameters used to create the images shown for each subject. A summary of the data comparing ARFI imaging displacements in ROIs based on MRI segmented plaque model contours >2 mm^2 is provided at the end of this section to highlight the key results for each subject.

A. Subject 1

Figure 3 shows spatially registered MRI, B-mode, and ARFI images of the right carotid artery in Subject 1. In Figure 3a, a transverse 2D TOF image (red imaging plane), longitudinal 2D B-mode image (green imaging plane), and 3D segmented MRI plaque model are shown relative to the CCA, ICA, and ECA of the 3D TOF derived arterial lumen volume rendering. The 3D segmented MRI plaque model is also shown in the same and rotated orientations in Figure 3b and Figure 3c, respectively, but without the TOF and B-mode information. The 3D segmented MRI plaque models in Figure 3a–c show a complex, heterogeneous plaque with lipid (yellow) and calcium (white) components embedded within the loose matrix (blue) material of normal arterial tissue. The plaque volume is dominated by a large calcium region (white arrow) with an adjacent lipid region (yellow arrow) on the left side of the ICA.

Figure 3d shows a single transverse 2D TOF image, acquired in the red imaging plane, with overlaid contours of the 3D segmented MRI plaque model. The green line indicates the intersection of the ultrasound imaging plane in which the longitudinal B-mode and ARFI images were acquired. Figure 3e shows a high quality 2D B-mode image that was displayed by the ultrasound scanner during the exam with two faint vertical lines indicating the lateral extent of the 2D ARFI imaging FOV. In B-mode imaging, the large plaque on the far wall of the CCA and ICA presents as a heterogeneous mass with a hypoechoic central region between the far wall and the more hyperechoic plaque top. Acoustic shadowing artifacts stemming from the center of the plaque and in the superior direction (i.e. towards the ICA) are observed in the underlying soft tissue.

Figure 3f shows the 2D B-mode image acquired in the green imaging plane with overlaid contours of the 3D segmented MRI plaque model, indicating composition, shown in solid lines. The coarseness of the 3D segmented MRI plaque model contours is reflective of the 2mm slice thickness of MRI in the longitudinal B-mode/ARFI imaging plane. Figure 3g shows the 2D ARFI image depicting the maximum axial displacements in μm overlaid on a 2D B-mode image. Dotted lines represent the ARFI ROIs derived from the segmented MRI plaque model contours shown in solid lines in Figure 3f. Small white arrows separating the low displacements of the arterial wall from the high displacements of the softer surrounding tissue indicate the stiff arterial wall boundaries in the ARFI image. White and yellow arrows in the MRI images (a, b, c, d, and f) indicate the same calcium and lipid regions of interest. The white box in Figure 3f and Figure 3g indicate the ARFI image FOV. Comparisons of

specific plaque features between ARFI imaging and MRI are referenced with respect to the lateral position indicated by the horizontal ruler in the white box.

A 16mm^2 calcium region (white arrow) identified by MRI in the far wall of Figure 3f presents as a region of uniformly low (0.57±0.17 μm) displacements in the ARFI image in Figure 3g. An 11 mm^2 MRI identified lipid region (yellow arrow) (Figure 3f) presents as a region with increased displacements (1.75±0.85μm) in the ARFI image (Figure 3g). In the far wall, two loose matrix components (4mm^2 and 2mm^2) identified by MRI present as regions of low displacement (0.60±0.28μm and 0.65±0.32 μm) on the left and right, respectively in the ARFI image (Figure 3g). Further below the lipid region are small (<2mm^2) loose matrix components in the MRI image (Figure 3f) that present as regions of low (<1μm) displacement in the ARFI image (Figure 3g). In the near wall, a 25mm^2 MRI identified region of loose matrix components (Figure 3f) presents as a region of uniformly low (0.71±0.21 μm) displacement in the ARFI image (Figure 3g). A 1mm^2 MRI identified lipid region at a lateral position of −0.25 cm observed in Figure 3f was unidentified in the ARFI image (Figure 3g) and presented as a region of low displacement similar in magnitude to that of the loose matrix components in the arterial wall.

Figure 4 shows high quality B-mode images (top row) and ARFI images (bottom row) that were acquired at different imaging angles and separated in time from Subject 1. While different in size and geometry, a region of increased displacement in the center of the plaque (pink arrow) surrounded by regions of low displacement is observed at three different imaging angles. In all cases, the shape and location of the region of increased displacement corresponds to a similarly sized hypoechoic region (green arrows) in the B-mode images.

B. Subject 2

Spatially registered MRI, B-mode, and ARFI images of the right carotid artery in Subject 2 are shown in Figure 5. The high quality B-mode image in Figure 2a indicates a large homogeneous plaque on the far wall of the CCA and ICA. In Figure 5a, there is good agreement between the 3D segmented MRI plaque model contours and the 2D B-mode image with a slight vertical offset of approximately 1 mm on the near wall at a lateral position of −0.25 cm. At a lateral position of −0.5 cm, a 1mm^2 calcium deposit in the MRI image (white arrow) is aligned vertically with an acoustic shadowing artifact, that was found during the ultrasound exam to be caused by the small focal plaque indicated by the pink arrow on the near wall of the ICA in the high quality B-mode image (Figure 2a).

The 3D segmented MRI plaque model contours in Figure 5a portray a 10mm^2 lipid pool (yellow arrow) extending laterally from −0.5 to 0.5 cm that is surrounded by otherwise loose matrix components in the far wall. In the ARFI image (Figure 5b), the location of this lipid pool corresponds to a region of increased displacement (1.01±0.28μm), extending laterally from −0.25 cm to 0.25 cm, that was observed in four acquisitions acquired at this imaging angle over a 4 min. period. Thin regions of low displacement (0.66±0.16μm and 0.79±0.18 μm, respectively) are observed between the soft region and the lumen – possibly representing a fibrous cap – and also between the soft region and the surrounding tissue below the arterial wall – which likely represents the stiff adventitial layer. These low

displacement regions in the ARFI image of Figure 5b spatially correspond to regions of loose matrix in the 3D segmented MRI plaque model contours shown in Figure 5a.

C. Subject 3

Figure 6 shows spatially registered MRI, B-mode, and ARFI images of the left carotid artery in Subject 3. The high quality B-mode image in Figure 2b shows plaque on the near and far walls of the ICA and a large focal plaque at the BIF that appears to cause the acoustic shadowing artifacts observed below the ECA. In Figure 6a, there is good agreement between the lumen, arterial wall, and plaque geometry of the 3D segmented MRI plaque model contours and the 2D B-mode image.

A MRI identified calcium region and a loose matrix region in the far wall in Figure 6a present as regions of similarly low displacement (0.87±0.18 μm and 0.85±0.27 μm, respectively) in the ARFI image in Figure 6b. More superior in the ICA, MRI (Figure 6a) indicates a 6mm^2 lipid region in the far wall centered laterally at −0.5 cm that corresponds to a region of slightly increased displacement (1.45±0.51 μm) in the ARFI image (Figure 6b). In the near wall, there is a mix of lipid, loose matrix, and calcium components in the 3D segmented MRI plaque model contours, with a 15 mm^2 lipid pool (yellow arrow) centered at 0.0 cm that presents in the ARFI image (Figure 6b) as a region of heterogeneous displacements (1.90±1.10μm). Despite large variance in displacements observed within this region, the focal regions of increased displacement (>3μm) located near the BIF (pink arrows in Figure 6b) were observed in five acquisitions acquired at an imaging angle of 240° over a 3 min. time period. In the near wall from 0.0 cm to −0.75 cm, ARFI imaging displacements of low magnitude (1.2±0.2μm and 1.1±0.21μm) were observed in MRI identified regions of lipid and loose matrix components, respectively.

D. Subject 4

Figure 7 shows spatially registered MRI, B-mode, and ARFI images of the left carotid artery in Subject 4. The high quality B-mode image in Figure 2c depicts a relatively homogeneous plaque on the far wall of the ICA associated with a large amount of acoustic shadowing underneath. There is relatively good agreement between the arterial wall and plaque geometry of the 3D segmented MRI plaque model contours and the 2D B-mode image in Figure 7a.

A 37mm^2 calcium region (white arrow) in the far wall of the ICA identified by MRI (Figure 7a) presents as a region of low displacements (0.89±0.52 μm) in ARFI imaging (Figure 7b) that is fairly homogeneous, except for a 1mm^2 localized region of increased displacements (4μm) located at 0.1 cm laterally. This small, high displacement region was observed in four ARFI images that were acquired in the same location, but approximately 30 sec. apart and is in close proximity to a 1mm^2 MRI-identified lipid region (yellow arrow) observed in Figure 7a. Another small MRI-identified lipid region (2mm^2) located at −0.25 cm in Figure 7a presents no differently than the low displacements within the rest of the plaque in the ARFI image in Figure 7b.

E. Subject 5

Figure 8 shows spatially registered MRI, B-mode, and ARFI images of the left carotid artery in Subject 5. In the high quality B-mode image (Figure 2d) a plaque (pink arrow) is clearly observed within the ECA. This particular plaque was not detected in MRI and is therefore not observed in the 3D segmented MRI plaque model contours in Figure 8a. There is good agreement between the geometry of the arterial walls in the 3D segmented MRI plaque model contours and the 2D B-mode image in Figure 8a.

Within the ARFI image FOV, the 3D segmented MRI plaque model contours in Figure 8a indicate the near wall of the ECA is dominated by an $11mm^2$ loose matrix component with a $3mm^2$ region of calcium at approximately −0.25 cm (white arrow). In the spatially registered 2D ARFI image (Figure 8b) both regions presents as areas of low displacement (0.91±0.37μm and 0.69±0.26μm, respectively). The $4mm^2$ plaque in the middle of the ECA (pink arrow) observed in the B-mode image at a lateral position of 0.0 cm (Figure 8a and Figure 2d) presents in the ARFI image (Figure 8b) as a concentrated region of high displacements >3μm. A thin region of low displacements (1.53±0.30μm) that corresponds to MRI identified loose matrix components – likely the stiff adventitial layer – separates the high displacement plaque from the increased displacements of the surrounding tissue beneath the far wall of the artery.

F. Summary

A summary comparing the mean and standard deviation of ARFI imaging displacements within ROIs based on 3D segmented MRI plaque model contours of varying composition > $2mm^2$ is shown in Figure 9 for each subject. Dotted line contours overlaying the preceding ARFI images (Figures 3, 5–8) represent the ARFI ROIs used for analysis.

While summary results from all subjects are shown together in Figure 9, note the force applied with ARFI imaging – which is unknown *in vivo* – is depth dependent and varies between subjects. Such variation may explain differences in the displacement magnitude observed between regions of similar composition in the near wall and the far wall in a single subject and also between subjects. For this reason, it is the relative difference in displacement magnitude of a region compared to surrounding regions within each subject that is most important.

IV. Discussion

This work presents preliminary *in vivo* human results comparing ARFI imaging derived carotid plaque stiffness with composition determined by spatially registered MRI. With no reported *in vivo* human validation of plaque characterization using ARFI imaging to date, this work provides early training data for future efforts and aids in the interpretation and possible clinical utility of the method. Additionally, the correspondence of increased ARFI displacements in regions identified as lipid in MRI is preliminary data that demonstrates the potential of ARFI imaging for identifying the elusive vulnerable plaque.

A. Plaque Stiffness (ARFI imaging) vs. Composition (MRI)

Results among five subjects with carotid artery plaques > 50% stenosis were reported. Normal loose matrix components identified by MRI presented as homogeneous, stiff regions of low displacement (typically ≈1μm) in ARFI imaging. MRI identified calcium components presented as regions of similarly low magnitude and were generally indistinguishable from loose matrix components in ARFI imaging.

Lipid pools >2 mm^2 were identified by MRI in three of the five subjects (Subject 1 - Figure 3, Subject 2 - Figure 5, and Subject 3 - Figure 6). In these cases, corresponding regions in spatially registered ARFI images presented as soft regions with mean displacements that were on average 1.8 times greater (Subject 1 = 2.9×, Subject 2 = 1.4×, Subject 3 = 1.2× in the near wall and 1.7× in the far wall) than displacements measured in stiffer, adjacent regions containing loose matrix components according to MRI (Figure 9). In Subject 1 (Figure 3), the regions of increased displacement in ARFI imaging presented as hypoechoic regions in B-mode imaging, whose presence has been related to the presence of ipsilateral neurological events [30,31]. No ARFI imaging soft region greater than 2mm^2 corresponded to regions with either loose matrix and/or calcium components according to MRI.

The contrast in mean ARFI imaging displacements between MRI identified regions of lipid compared to calcium and loose matrix components was < 2 for all subjects except Subject 1 (Figure 9). In an *ex vivo* popliteal artery, Trahey et al. [26] reported a contrast value of 1.5 between a pathologically confirmed lipid core and a calcium region. These values are lower than those reported by Dumont et al. [?] in custom-made, arterial tissue-mimicking phantoms, where the displacements of a soft inclusion with a Young's Modulus (E) of E = 19.7 kPa were three times higher than those measured in the stiffer background (E = 121.8 kPa). In finite element simulations the contrast was most dependent upon stiffness of the lipid pool, ranging from a maximum of ≈8 for a lipid stiffness of E_{lipid} = 0.5 kPa to a minimum of ≈1 for E_{lipid} = 50kPa with E_{wall} = 1000 kPa [23].

B. Challenges & Limitations

Several challenges and limitations should be considered when interpreting the results of this preliminary study. First, despite observed differences in the mean ARFI displacements, the increased variance of ARFI displacements within MRI-identified lipid regions indicates the clear separation of components may be difficult with ARFI imaging in some patients (Figure 9). Unfortunately, the small sample size is not sufficient to show statistical significance and future studies involving more subjects are required to truly validate the use of ARFI imaging for carotid plaque characterization. Towards assuring confidence in the results, however, a repeatability study of ARFI imaging was performed by comparing images acquired at the same location on a qualitative basis. While not shown for conciseness, the ARFI images were spatially and temporally consistent across multiple acquisitions. Additionally, lack of motion in "non-push" ARFI frames acquired with each acquisition provided confidence that regions of varying stiffness did not arise from non-ARFI induced effects. Such stability and confidence in the results made it necessary to only perform the time-consuming manual registration for a single B-mode/ARFI image pair, as additional datasets did not add any new information.

Differences in the geometry of specific features observed between MRI and ARFI imaging may be attributed to a number of factors, including possible differences in sensitivity of the techniques to regions of varying composition. An increased lipid pool stiffness may, for example, lead to decreased sensitivity of ARFI imaging and that may explain the regions of low displacement observed in the 15mm^2 lipid pool identified by MRI in the near wall of Subject 3.

Differences in the resolution of MRI and ARFI imaging may also account for dissimilarity between observed features. The longitudinal imaging plane of the B-mode and ARFI images is the worst dimension for MRI resolution, with the 2mm slice thickness of the T1W, PDW, and T2W accounting for the coarseness of the segmented MRI contours overlaid on the B-mode images in this study. The low resolution of MRI in the longitudinal plane may also explain why the 4 mm^2 plaque clearly visualized in Subject 5 (Figure 8) with B-mode imaging that presented as a temporally and spatially stable region of increased displacement in ARFI imaging was not detected by MRI. The pronounced effects of the large MRI slice thickness could be reduced by collecting the MRI and ultrasound imaging data in the same imaging plane. Currently however, the semi-automated MRI segmentation method used in this study does not support MRI images acquired in the longitudinal orientation. Additionally, while acquiring ARFI images in the transverse orientation is possible, future work is needed to investigate the source of reduced image quality in the transverse ARFI images acquired, but not included, in this study before this approach is viable.

The smallest size lipid pool that can be detected with ARFI imaging is unknown. The ARFI segmentation analysis only included MRI regions > 2 mm^2, based on earlier studies showing high sensitivity and specificity of MRI plaque characterization in regions of this size [17]. While the resolution of ARFI imaging, which depends on parameters of both the push beam and also the tracking beam, is in general comparable with the resolution of B-mode imaging [?], further studies investigating both contrast-to-noise ratio and resolution of small structures, such as lipid pools, *in vivo* is warranted.

The millimeter-scale size of the plaque components, means that subtle mis-registration errors may also explain observed differences. While adjusting the six parameters needed to define the location of a single plane made manual registration of the B-mode image within the 3D TOF MRI volume a somewhat tedious task, the unique geometry of the carotid artery and plaques provided sufficient information to guide these efforts. Fine tuning of the spatial transformations suggested the registration was accurate within 5° in rotation and 1mm in translation. Possible sources of mis-registration include not only differences in resolution of the B-mode and MRI data, but also possible variation in arterial geometry resulting from patient motion and/or differences in the neck position during the ultrasound and MRI exams.

Good agreement observed between 3D segmented MRI plaque model contours overlaid on 2D B-mode images in each subject is strong evidence to support the accuracy of the manual registration performed herein. In all subjects, mis-registration of obvious features, such as the arterial wall–lumen interface, between B-mode and MRI was <1mm. Further confidence in the registration is provided by the spatial alignment of acoustic shadowing artifacts,

indicative of calcium, in the B-mode images of Subjects 1–4 (Figures 3, 5–7) with regions identified as calcium in MRI.

Given the small size of many plaque features, differences in the resolution of MRI and B-mode/ARFI imaging and the potential for mis-registration errors makes a strict 1:1 comparison between MRI composition and ARFI imaging plaque stiffness difficult in this study. Interested in the comparison of larger features, we allowed <1mm non-rigid, manual adjustment of the MRI segmented contours in defining ARFI ROIs to reduce these effects while minimizing subjectivity in choosing the specific regions used for analysis. Automated MR and ultrasound image registration [32] may help further reduce mis-registration while improvements in the spatial resolution of MRI may make a more detailed comparison feasible.

The limitation of 2D ultrasound imaging for characterizing the complicated 3D nature of atherosclerotic plaque burden was noted in this study. As observed in Figure 3d, the 2D ultrasound imaging plane (green plane) interrogates a limited region of the plaque; making it entirely possible to miss important plaque features such as lipid pools. The spatial and temporal repeatability of ARFI imaging observed in this study suggests that only a single acquisition is required at each location/angle, however, multiple locations/angles would be required to fully characterize the complex plaque. Future studies of this kind therefore should work towards 2D sweeping techniques and/or 3D ARFI imaging methods.

C. Clinical Implications & Utility

Ultrasound's ease of use, low cost, safety, noninvasive nature, and relatively short scan time make ARFI imaging more feasible for routine screening exams than other imaging modalities. Unlike MRI and CT imaging, however, the results in this study indicate ARFI imaging cannot differentiate calcium from normal loose matrix components in plaque tissue. While calcium is an important indicator of atherosclerosis [33], studies have shown in aorta specimens that calcium quantity does not predict the likelihood of a plaque to rupture [?]. More so, recent evidence from MRI has shown the presence of a lipid pool alone is an important predictor of cardiovascular events [34]. The low contrast between the displacements of MRI identified lipid regions and adjacent arterial tissue may place an upper limit on the stiffness of lipid pools that can be identified by ARFI imaging. However, with increasing contrast indicating a softer lipid pool, which is more prone to rupture, it is possible the contrast in ARFI imaging displacements may provide important prognostic information related to plaque vulnerability. Certainly however, future studies correlating ARFI imaging derived plaque stiffness with clinical events in a large number of patients are needed to assess the true clinical utility of the method.

Acknowledgments

This work was supported by NIH grants R01HL075485and R37HL096023 from the NHLBI.

References

1. Spagnoli LG, Mauriello A, Sangiorgi G, Fratoni S, Bonanno E, Schwartz RS, Piepgras DG, Pistolese R, Ippoliti A, Holmes DR. Extracranial thrombotically active carotid plaque as a risk

factor for ischemic stroke. JAMA : the journal of the American Medical Association. 2004 Oct; 292(15):1845–1852.

2. Go AS, Mozaffarian D, Roger VL, Benjamin EJ, Berry JD, Borden WB, Bravata DM, Dai S, Ford ES, Fox CS, Franco S, Fullerton HJ, Gillespie C, Hailpern SM, Heit Ja, Howard VJ, Huffman MD, Kissela BM, Kittner SJ, Lackland DT, Lichtman JH, Lisabeth LD, Magid D, Marcus GM, Marelli A, Matchar DB, McGuire DK, Mohler ER, Moy CS, Mussolino ME, Nichol G, Paynter NP, Schreiner PJ, Sorlie PD, Stein J, Turan TN, Virani SS, Wong ND, Woo D, Turner MB. Heart disease and stroke statistics–2013 update: a report from the American Heart Association. Circulation. 2013 Jan; 127(1):e6–e245. [Online]. Available: http://www.ncbi.nlm.nih.gov/pubmed/23239837. [PubMed: 23239837]
3. Casscells W, Naghavi M, Willerson JT. Vulnerable atherosclerotic plaque: a multifocal disease. Circulation. 2003 Apr; 107(16):2072–2075. [PubMed: 12719287]
4. Lee RT, Libby P. The Unstable Atheroma. Arteriosclerosis, Thrombosis, and Vascular Biology. 1997; 17(10):1859–1867.
5. Felton CV, Crook D, Davies MJ, Oliver M. Relation of Plaque Lipid Composition and Morphology to the Stability of Human Aortic Plaques. Arteriosclerosis, Thrombosis, and Vascular Biology. 1997; 17(7):1337–1345.
6. van der Wal AC, Becker AE. Atherosclerotic plaque rupture–pathologic basis of plaque stability and instability. Cardiovascular research. 1999 Feb; 41(2):334–344. [PubMed: 10341833]
7. Redgrave JNE, Lovett JK, Gallagher PJ, Rothwell PM. Histological assessment of 526 symptomatic carotid plaques in relation to the nature and timing of ischemic symptoms: the Oxford plaque study. Circulation. 2006 May; 113(19):2320–2328. [PubMed: 16651471]
8. Loree HM, Tobias BJ, Gibson LJ, Kamm RD, Small DM, Lee RT. Mechanical properties of model atherosclerotic lesion lipid pools. Arteriosclerosis, Thrombosis, and Vascular Biology. 1994 Feb; 14(2):230–234.
9. Lee RT, Grodzinsky AJ, Frank EH, Kamm RD, Schoen FJ. Structure-dependent dynamic mechanical behavior of fibrous caps from human atherosclerotic plaques. Circulation. 1991; 83(5): 1764–1770. [PubMed: 2022029]
10. Keeny SM, Richardson PD. Stress analysis of atherosclerotic arteries. Eng Med Biol Soc; Proceedings of the IEEE Ninth Annual Conference. 1987:1484–1485.
11. Li Z-Y, Howarth S, Trivedi RA, U-King-Im JM, Graves MJ, Brown A, Wang L, Gillard JH. Stress analysis of carotid plaque rupture based on in vivo high resolution MRI. Journal of Biomechanics. 2006; 39(14):2611–2622. [PubMed: 16256124]
12. Sanz J, Fayad ZA. Imaging of atherosclerotic cardiovascular disease. Nature. 2008 Feb; 451(7181): 953–957. [PubMed: 18288186]
13. Waxman S, Ishibashi F, Muller JE. Detection and Treatment of Vulnerable Plaques and Vulnerable Patients. Circulation. 2006 Nov; 114(22):2390–2411. [PubMed: 17130356]
14. Hatsukami TS, Yuan C. MRI in the early identification and classification of high-risk atherosclerotic carotid plaques. Imaging Medicine. 2010; 2(1):63–75.
15. Hatsukami TS, Ross R, Polissar NL, Yuan C. Visualization of Fibrous Cap Thickness and Rupture in Human Atherosclerotic Carotid Plaque In Vivo With High-Resolution Magnetic Resonance Imaging. Circulation. 2000 Aug; 102(9):959–964. [PubMed: 10961958]
16. Zhao X, Underhill H, Yuan C, Oikawa M, Dong L, Ota H, Hatsukami T, Wang Q, Ma L, Cai J. Minimization of MR contrast weightings for the comprehensive evaluation of carotid atherosclerotic disease. Invest Radiol. 2010; 45(1):36–41. [PubMed: 19996759]
17. Saam T, Ferguson MS, Yarnykh VL, Takaya N, Xu D, Polissar NL, Hatsukami TS, Yuan C. Quantitative evaluation of carotid plaque composition by in vivo MRI. Arteriosclerosis, thrombosis, and vascular biology. 2005 Jan; 25(1):234–239.
18. Takaya N, Yuan C, Chu B, Saam T, Underhill H, Cai J, Tran N, Polissar NL, Isaac C, Ferguson MS, Garden Ga, Cramer SC, Maravilla KR, Hashimoto B, Hatsukami TS. Association between carotid plaque characteristics and subsequent ischemic cerebrovascular events: a prospective assessment with MRI–initial results. Stroke. 2006 Mar; 37(3):818–823. [PubMed: 16469957]

19. Yuan C, Mitsumori LM, Beach KW, Maravilla KR. Carotid Atherosclerotic Plaque: Noninvasive MR Characterization and Identification of Vulnerable Lesions. Radiology. 2001; (6):285–299. [PubMed: 11687667]
20. Cury R, Houser S, Furie K, Stone J, Olgivy C, Sherwood J, Muller J, Brady T, Hinton D. Vulnerable plaque detection by 3.0 tesla magnetic resonance imaging. Invest Radiol. 2006; 41(2): 112–115. [PubMed: 16428981]
21. Doherty JR, Trahey GE, Nightingale KR, Palmeri ML. Acoustic Radiation Force Elasticity Imaging in Diagnostic Ultrasound. IEEE Trans Ultrason Ferroelect Freq Contr. 2013; 60(4):685–701.
22. Nightingale KR, Palmeri ML, Nightingale RW, Trahey GE. On the Feasibility of Remote Palpation Using Acoustic Radiation Force. J Acoust Soc Am. 2001; 110(1):625–634. [PubMed: 11508987]
23. Doherty JR, Dumont DM, Trahey GE, Palmeri ML. Acoustic radiation force impulse imaging of vulnerable plaques: a finite element method parametric analysis. Journal of Biomechanics. 2013; 46(1):83–90. [PubMed: 23122224]
24. Behler RH, Nichols TC, Zhu H, Merricks EP, Gallippi CM. ARFI imaging for noninvasive material characterization of atherosclerosis. Part II: toward in vivo characterization. Ultrasound Med Biol. 2009; 35(2):278–295. [PubMed: 19026483]
25. Dumont DM, Behler RH, Nichols TC, Merricks EP, Gallippi CM. ARFI imaging for noninvasive material characterization for atherosclerosis. Ultrasound Med Biol. 2006; 32(11):1117–1703.
26. Trahey GE, Palmeri ML, Bentley RC, Nightingale KR. Acoustic radiation force impulse imaging of the mechanical properties of arteries: in vivo and ex vivo results. Ultrasound Med Biol. 2004 Sep; 30(9):1163–1171. [PubMed: 15550320]
27. Dahl JJ, Dumont DM, Allen JD, Miller EM, Trahey GE. Acoustic radiation force impulse imaging for noninvasive characterization of carotid artery atherosclerotic plaques: a feasibility study. Ultrasound Med Biol. 2009; 35(5):707–716. [PubMed: 19243877]
28. Doherty JR, Dahl JJ, Trahey GE. Harmonic Tracking of Acoustic Radiation Force Induced Displacements. IEEE Trans Ultrason Ferroelect Freq Contr. 2013; 60(11):2347–2358.
29. Hsu SJ, Bouchard RR, Dumont DM, Wolf PD, Trahey GE. In vivo assessment of myocardial stiffness with acoustic radiation force impulse imaging. Ultrasound Med Biol. 2007 Nov; 33(11): 1706–1719. [PubMed: 17698282]
30. Mathiesen EB, Bonaa KH, Joakimsen O. Echolucent Plaques Are Associated With High Risk of Ischemic Cerebrovascular Events in Carotid Stenosis : The Tromso Study. Circulation. 2001 May; 103(17):2171–2175. [Online]. Available: http://circ.ahajournals.org/cgi/doi/10.1161/01.CIR.103.17.2171. [PubMed: 11331258]
31. Christodoulou C, Pattichis C, Pantziaris M, Nicolaides A. Texture-based classification of atherosclerotic carotid plaques. IEEE Trans Med Imaging. 2003; 22(7):902–912. [PubMed: 12906244]
32. Porter B, Rubens D, Strang J, Smith J, Totterman S, Parker K. Three-dimensional registration and fusion of ultrasound and MRI using major vessels as fiducial markers. IEEE Trans Med Imaging. 2001; 20(4):354–359. [PubMed: 11370902]
33. Wexler L, Brundage B, Crouse J, Detrano R, Fuster V, Maddahi J, Rumberger J, Stanford W, White R, Taubert K. Coronary Artery Calcification: Pathophysiology, Epidemiology, Imaging Methods, and Clinical Implications. Circulation. 1996; 94:1175–1192. [PubMed: 8790070]
34. Zavodni AEH, Wasserman BA, McClelland RL, Gomes AS, Folsom AR, Polak JF, Lima JaAC, Bluemke DA. Carotid Artery Plaque Morphology and Composition in Relation to Incident Cardiovascular Events: The Multi-Ethnic Study of Atherosclerosis (MESA). Radiology. 2014 In Press, [Online]. Available: http://pubs.rsna.org/doi/abs/10.1148/radiol.14131020.

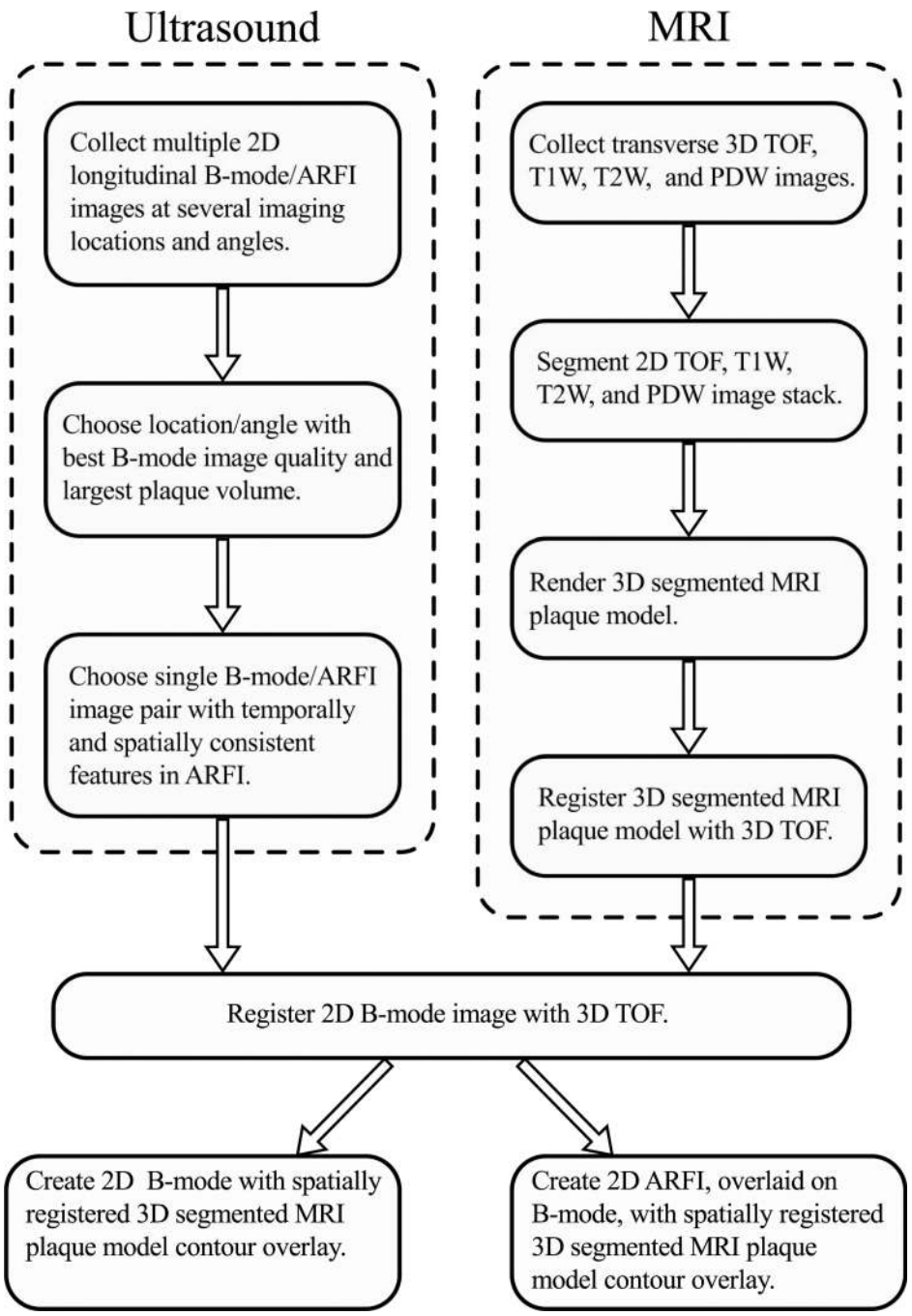

Fig. 1.
Overview of ultrasound and MR image registration.

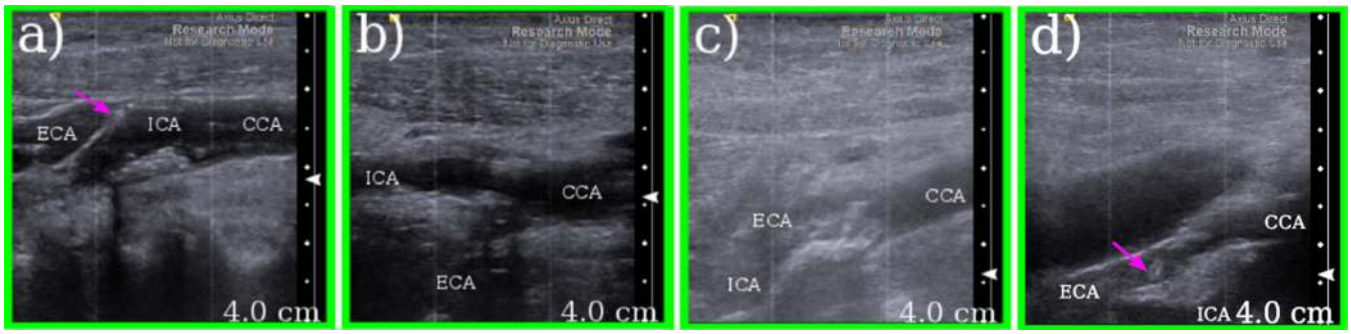

Fig. 2.

High quality B-mode images displayed by the ultrasound scanner during the exam for: a) Subject 2 (Figure 5), b) Subject 3 (Figure 6), c) Subject 4 (Figure 7), and d) Subject 5 (Figure 8). The focal depth used for each image is indicated by the small white triangle on the depth axis located on the right side of each image. The faint vertical lines in each image indicate the 2D ARFI imaging FOV for each acquisition.

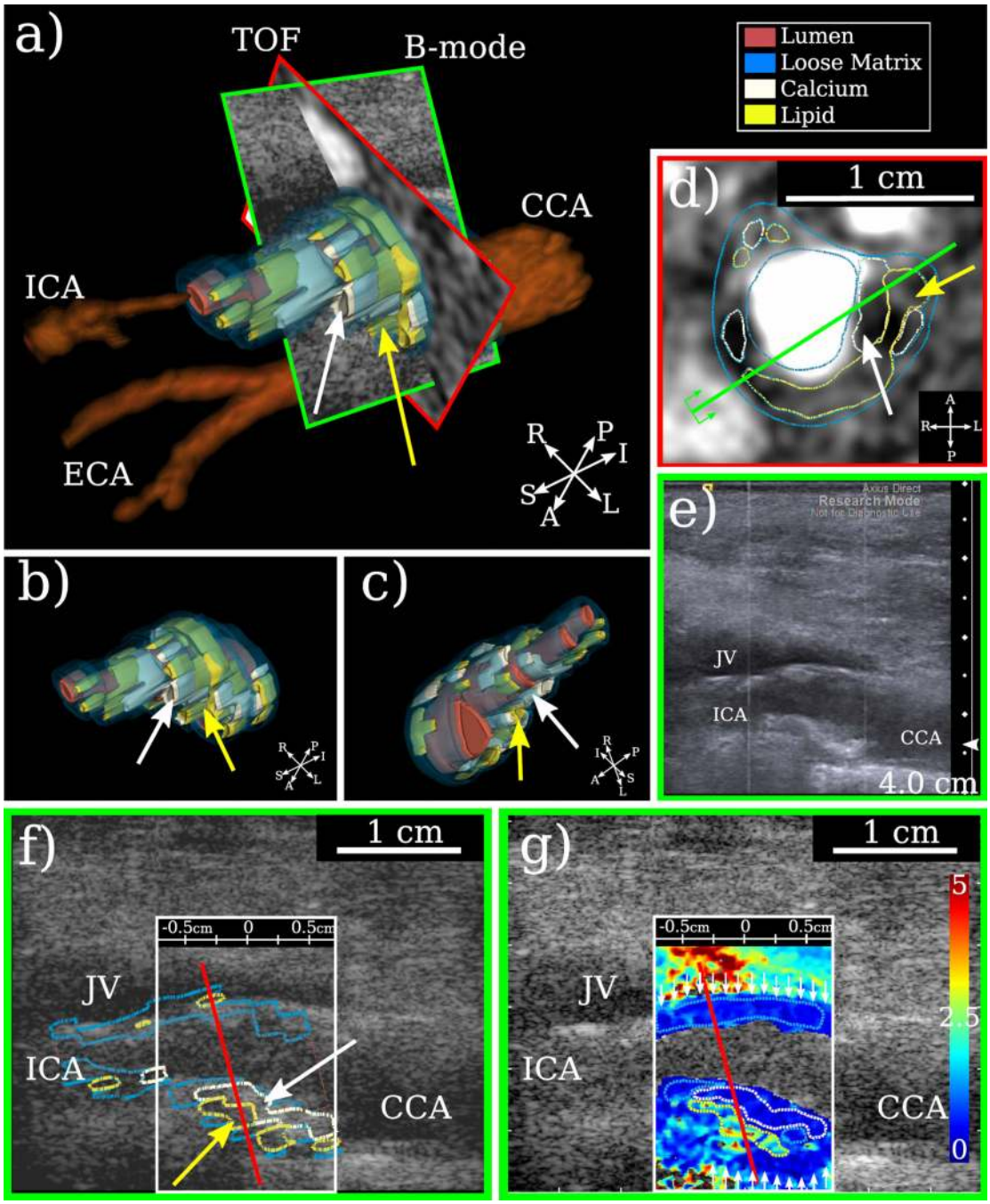

Fig. 3.

Subject 1, spatially registered *in vivo* MRI and ultrasound images. a) 2D TOF image (red plane), 2D B-mode image (green plane), and 3D segmented MRI plaque model sbowing composition with 3D TOF arterial lumen volume. b) 3D segmented MRI plaque model. c) 3D segmented MRI plaque model in rotated orientation. d) 2D TOF with overlaid 3D segmented MRI plaque model contours. e) High quality 2D B-mode image. f) 2D B-mode with overlaid 3D segmented MRI plaque model contours (solid lines). g) 2D ARFI depicting

axial displacements in μm overlaid on 2D B-mode with ARFI ROIs (dotted lines) derived from segmented MRI contours.

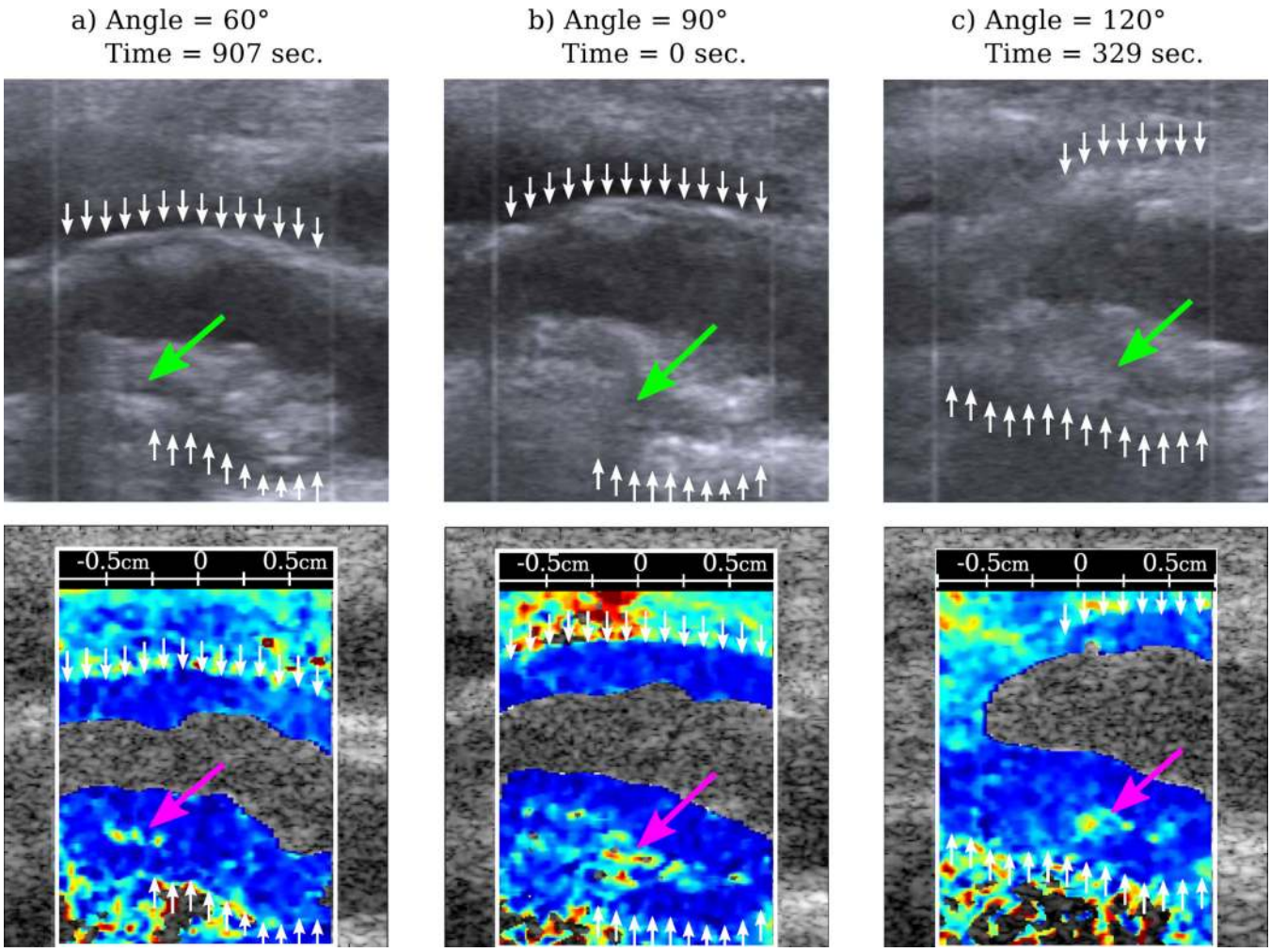

Fig. 4.

High-quality B-mode images (top row) and ARFI images (bottom row) of the carotid artery plaque in Subject 1 (Figure 3) that were acquired at different imaging angles and separated in time. The times listed are in reference to the acquisition time of the image shown in b).

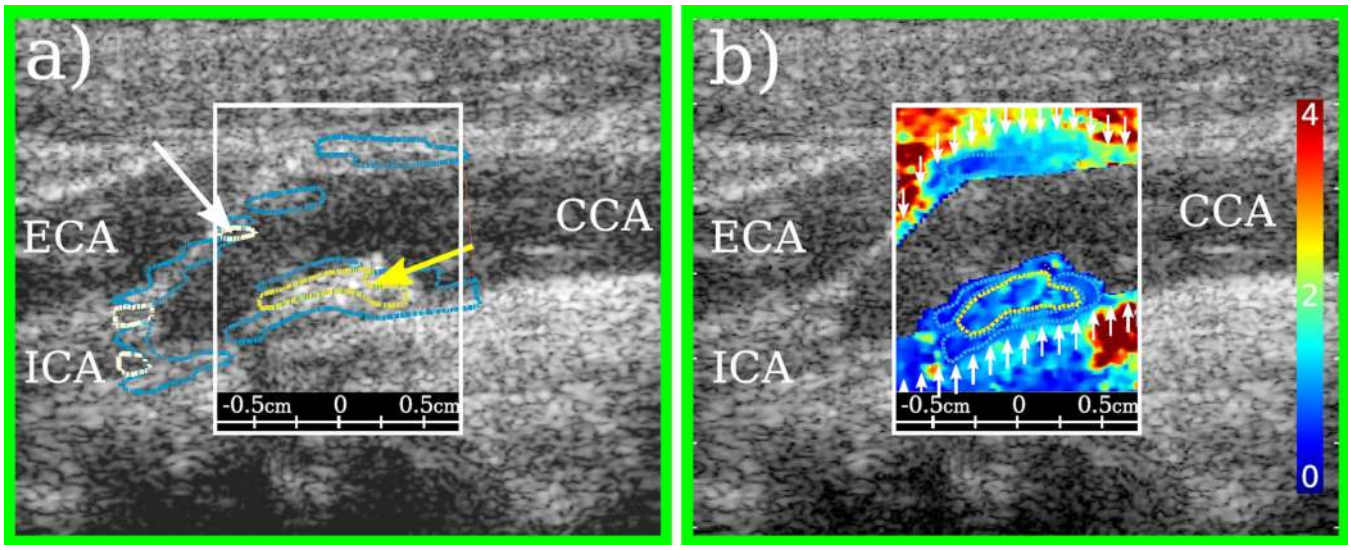

Fig. 5.

Subject 2, spatially registered *in vivo* MRI and ultrasound images. a) 2D B-mode with overlaid 3D segmented MRI plaque model contours (solid lines). b) 2D ARFI depicting axial displacements in μm overlaid on 2D B-mode with ARFI ROIs (dotted lines) derived from 3D segmented MRI plaque model contours.

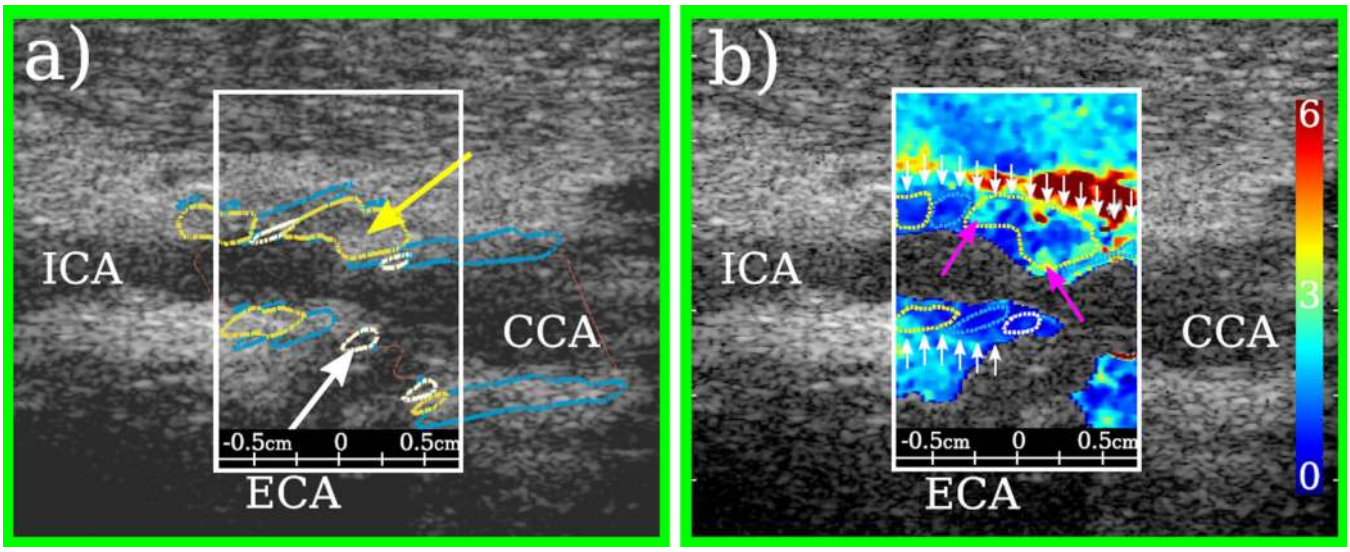

Fig. 6.

Subject 3, spatially registered *in vivo* MRI and ultrasound images. a) 2D B-mode with overlaid 3D segmented MRI plaque model contours. b) 2D ARFI depicting axial displacements in μm overlaid on 2D B-mode with ARFI ROIs (dotted lines) derived from 3D segmented MRI plaque model contours.

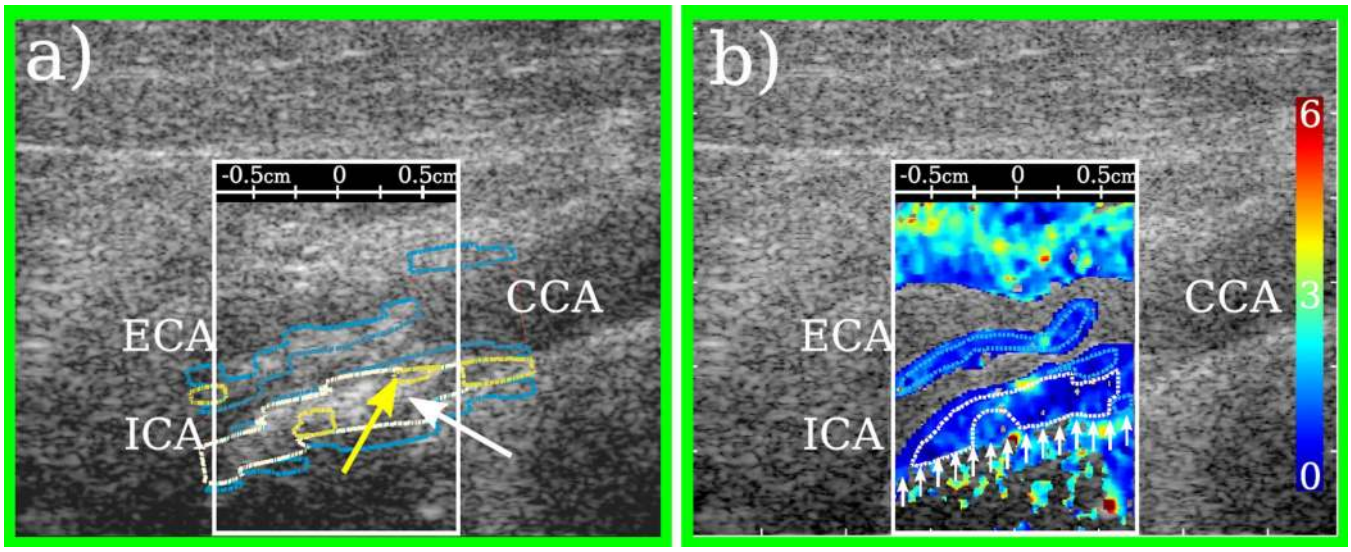

Fig. 7.

Subject 4, spatially registered *in vivo* MRI and ultrasound images. a) 2D B-mode with overlaid 3D segmented MRI plaque model contours. b) 2D ARFI depicting axial displacements in μm overlaid on 2D B-mode with ARFI ROIs (dotted lines) derived from 3D segmented MRI plaque model contours.

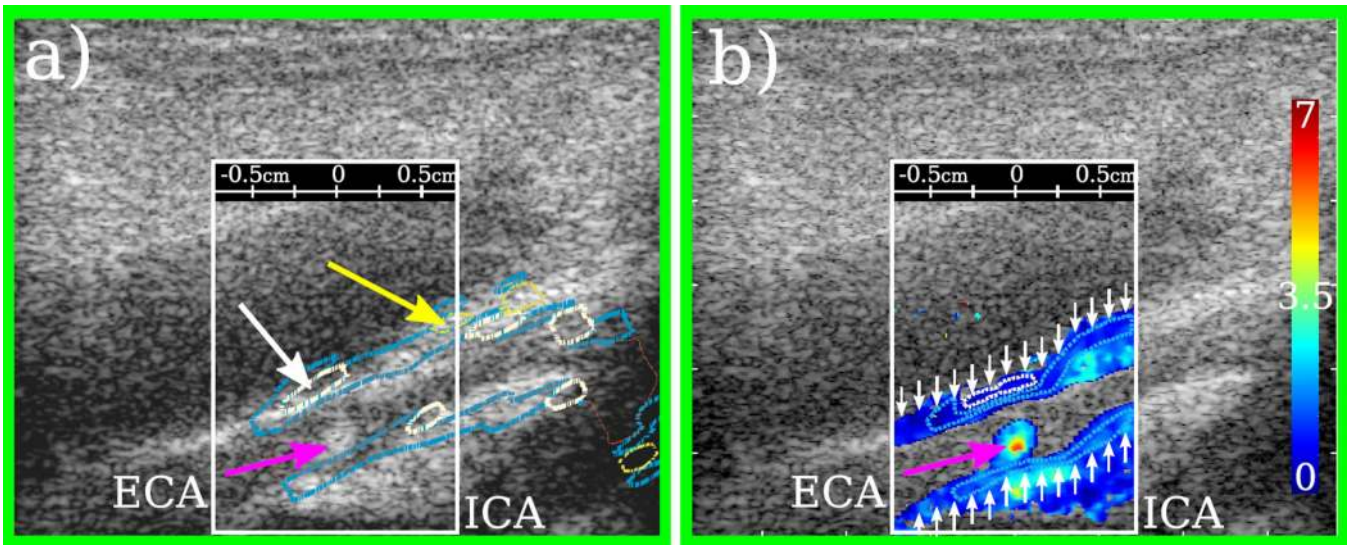

Fig. 8.

Subject 5, spatially registered *in vivo* MRI and ultrasound images. a) 2D B-mode with overlaid 3D segmented MRI plaque model contours. b) 2D ARFI depicting axial displacements in μm overlaid on 2D B-mode with ARFI ROIs (dotted lines) derived from 3D segmented MRI plaque model contours.

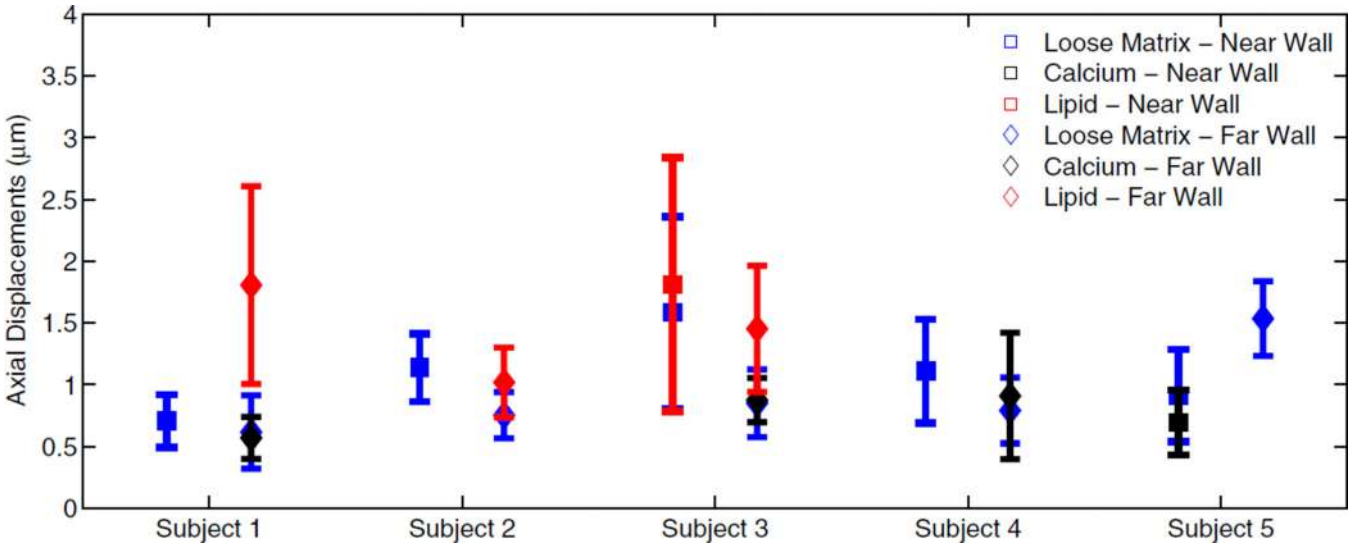

Fig. 9.

Mean and standard deviation of ARFI imaging displacements in ROIs based on MRI-derived contours of loose matrix, lipid, and calcium components in the near and far wall of each subject.

TABLE I

In vivo study population

Subject	Age	Sex (M/F)	Symptomatic (Y/N)	Plaque Location
1	68	M	N	Left BIF/ICA
2	84	F	N	Right BIF/ICA
3	80	F	Y	Left BIF/ICA
4	66	M	Y	Right BIF/ICA
5	72	F	N	Left ECA

ICA = Internal carotid artery, ECA = External carotid artery, BIF = carotid bifurcation

TABLE II

B-mode & ARFI imaging pulse characteristics

B-mode Imaging		Frequency (MHz)	4.0 PI Transmit, 8.0 (2nd Harmonic) Receive
		Pulse Duration (μsec)	0.250
		Transmit *F*/#	2.0
		Beam Spacing (mm)	0.154
ARFI Imaging	Push Beam	Frequency (MHz)	4.0
		Pulse Duration (μsec)	150
		Transmit *F*/#	3.0
		Beam Spacing (mm)	0.308
	Track Beam	Frequency (MHz)	4.0 PI Transmit, 8.0 (2nd Harmonic) Receive
		Pulse Duration (μsec)	0.250
		Transmit *F*/#	2.0
		Beam Spacing (mm)	0.308

PI = Pulse Inversion

TABLE III

MRI acquisition parameters

Scan	Repetition Time (msec)	Echo Time (msec)	Slice Thickness (mm)	Echo Train Length	Approx. Scan Time (min.)
3D TOF [1]	23	3.5	0.5	1	4
T1W DIR [2,3]	800	9	2.0	14	10
PDW [2,4]	Gated	20	2.0	6	6
T2W [2,4]	Gated	40	2.0	8	5

TOF=Time-of-flight, T1W=T1-weighted, DIR=Double Inversion Recovery, PDW= Proton density-weighted, T2W=T2-weighted

[1] Matrix Size = 512 × 512

[2] Matrix Size = 256 × 256

[3] DIR Inversion Time set to ‘Auto’ and determined by R-wave to R-wave interval (R–R)

[4] Cardiac Gating set to 3 R–R

TABLE IV

B-mode & ARFI image parameters

Subject	Focal Depth (cm)	Imaging Angle (°)	ARFI temporal window (msec)	ARFI NCC threshold
1	3.4	90	0.25–1.05	0.98
2	2.2	140	0.25–0.65	0.99
3	2.4	240	0.25–0.65	0.95
4	3.4	240	0.25–0.65	0.98
5	3.4	270	0.25–0.65	0.99